





























In the format provided by the authors and unedited.

# The seismicity of Mars

D. Giardini <sup>1</sup>✉, P. Lognonné <sup>2,3</sup>, W. B. Banerdt <sup>4</sup>, W. T. Pike<sup>5</sup>, U. Christensen<sup>6</sup>, S. Ceylan <sup>1</sup>, J. F. Clinton <sup>7</sup>, M. van Driel<sup>1</sup>, S. C. Stähler <sup>1</sup>, M. Böse<sup>1,7</sup>, R. F. Garcia<sup>8</sup>, A. Khan<sup>1,9</sup>, M. Panning<sup>4</sup>, C. Perrin <sup>2</sup>, D. Banfield <sup>10</sup>, E. Beucler <sup>11</sup>, C. Charalambous <sup>5</sup>, F. Euchner <sup>1</sup>, A. Horleston <sup>12</sup>, A. Jacob<sup>2</sup>, T. Kawamura<sup>2</sup>, S. Kedar<sup>4</sup>, G. Mainsant <sup>8</sup>, J.-R. Scholz <sup>6</sup>, S. E. Smrekar <sup>4</sup>, A. Spiga <sup>3,13</sup>, C. Agard<sup>14</sup>, D. Antonangeli<sup>15</sup>, S. Barkaoui<sup>2</sup>, E. Barrett<sup>4</sup>, P. Combes <sup>14</sup>, V. Conejero<sup>2</sup>, I. Daubar<sup>16</sup>, M. Drilleau<sup>2</sup>, C. Ferrier<sup>14</sup>, T. Gabsi<sup>2</sup>, T. Gudkova<sup>17</sup>, K. Hurst<sup>4</sup>, F. Karakostas<sup>18</sup>, S. King <sup>19</sup>, M. Knapmeyer <sup>20</sup>, B. Knapmeyer-Endrun <sup>21</sup>, R. Llorca-Cejudo<sup>14</sup>, A. Lucas <sup>2</sup>, L. Luno<sup>14</sup>, L. Margerin<sup>22</sup>, J. B. McClean<sup>5</sup>, D. Mimoun <sup>8</sup>, N. Murdoch<sup>8</sup>, F. Nimmo <sup>23</sup>, M. Nonon<sup>14</sup>, C. Pardo <sup>2</sup>, A. Rivoldini<sup>24</sup>, J. A. Rodriguez Manfredi <sup>25</sup>, H. Samuel<sup>2</sup>, M. Schimmel <sup>26</sup>, A. E. Stott<sup>5</sup>, E. Stutzmann<sup>2</sup>, N. Teanby <sup>12</sup>, T. Warren<sup>27</sup>, R. C. Weber<sup>28</sup>, M. Wieczorek<sup>29</sup> and C. Yana <sup>14</sup>

<sup>1</sup>Institute of Geophysics, Department of Earth Sciences, ETH Zurich, Zurich, Switzerland. <sup>2</sup>Université de Paris, Institut de Physique du Globe de Paris, CNRS, Paris, France. <sup>3</sup>Institut Universitaire de France, Paris, France. <sup>4</sup>Jet Propulsion Laboratory, California Institute of Technology, Pasadena, CA, USA. <sup>5</sup>Department of Electrical and Electronic Engineering, Imperial College London, London, UK. <sup>6</sup>Max Planck Institute for Solar System Research, Göttingen, Germany. <sup>7</sup>Swiss Seismological Service (SED), ETH Zurich, Zurich, Switzerland. <sup>8</sup>Institut Supérieur de l'Aéronautique et de l'Espace SUPAERO, Toulouse, France. <sup>9</sup>Institute of Theoretical Physics, University of Zurich, Zurich, Switzerland. <sup>10</sup>Cornell Center for Astrophysics and Planetary Science, Cornell University, Ithaca, NY, USA. <sup>11</sup>Laboratoire de Planétologie et Géodynamique, Univ. Nantes, Univ. Angers, CNRS, Nantes, France. <sup>12</sup>School of Earth Sciences, University of Bristol, Bristol, UK. <sup>13</sup>Laboratoire de Météorologie Dynamique, Sorbonne University, Paris, France. <sup>14</sup>Centre National d'Etudes Spatiales, Toulouse, France. <sup>15</sup>Institut de Minéralogie, de Physique des Matériaux et de Cosmochimie, Muséum National d'Histoire Naturelle, Sorbonne University, Paris, France. <sup>16</sup>Department of Earth, Environmental and Planetary Sciences, Brown University, Providence, RI, USA. <sup>17</sup>Schmidt Institute of Physics of the Earth, Russian Academy of Sciences, Moscow, Russia. <sup>18</sup>Department of Geology, University of Maryland, College Park, MD, USA. <sup>19</sup>Department of Geosciences, Virginia Polytechnic Institute, Blacksburg, VA, USA. <sup>20</sup>DLR Institute of Planetary Research, Berlin, Germany. <sup>21</sup>Bensberg Observatory, University of Cologne, Bergisch Gladbach, Germany. <sup>22</sup>Institut de Recherche en Astrophysique et Planétologie, Université Toulouse III Paul Sabatier, CNRS, CNES, Toulouse, France. <sup>23</sup>Dept. of Earth and Planetary Sciences, University of California Santa Cruz, Santa Cruz, CA, USA. <sup>24</sup>Royal Observatory of Belgium, Brussels, Belgium. <sup>25</sup>Centro de Astrobiología—Instituto Nacional de Técnica Aeroespacial, Madrid, Spain. <sup>26</sup>The Institute of Earth Sciences Jaume Almera of the Spanish Scientific Research Council (ICTJA-CSIC), Barcelona, Spain. <sup>27</sup>University of Oxford, Department of Physics, Oxford, UK. <sup>28</sup>NASA Marshall Space Flight Center, Huntsville, AL, USA. <sup>29</sup>Université Côte d'Azur, Observatoire de la Côte d'Azur, CNRS, Laboratoire Lagrange, Nice, France.

✉e-mail: [domenico.giardini@erdw.ethz.ch](mailto:domenico.giardini@erdw.ethz.ch)

## Supplementary Information for

### “The Seismicity of Mars”

D. Giardini<sup>1</sup>, P. Lognonné<sup>2,3</sup>, W. B. Banerdt<sup>4</sup>, W. T. Pike<sup>5</sup>, U. Christensen<sup>6</sup>, S. Ceylan<sup>1</sup>, J. F. Clinton<sup>7</sup>, M. van Driel<sup>1</sup>, S. C. Stähler<sup>1</sup>, M. Böse<sup>1,7</sup>, R. F. Garcia<sup>8</sup>, A. Khan<sup>1,9</sup>, M. Panning<sup>4</sup>, C. Perrin<sup>2</sup>, D. Banfield<sup>10</sup>, E. Beucler<sup>11</sup>, C. Charalambous<sup>5</sup>, F. Euchner<sup>1</sup>, A. Horleston<sup>12</sup>, A. Jacob<sup>2</sup>, T. Kawamura<sup>2</sup>, S. Kedar<sup>4</sup>, G. Mainsant<sup>8</sup>, J.-R. Scholz<sup>6</sup>, S. E. Smrekar<sup>4</sup>, A. Spiga<sup>3,13</sup>, C. Agard<sup>14</sup>, D. Antonangeli<sup>15</sup>, S. Barkaoui<sup>2</sup>, E. Barrett<sup>6</sup>, P. Combes<sup>14</sup>, V. Conejero<sup>2</sup>, I. Daubar<sup>16</sup>, M. Drilleau<sup>2</sup>, C. Ferrier<sup>14</sup>, T. Gabsi<sup>2</sup>, T. Gudkova<sup>17</sup>, K. Hurst<sup>4</sup>, F. Karakostas<sup>18</sup>, S. King<sup>19</sup>, M. Knapmeyer<sup>20</sup>, B. Knapmeyer-Endrun<sup>21</sup>, R. Llorca-Cejudo<sup>14</sup>, A. Lucas<sup>2</sup>, L. Luno<sup>14</sup>, L. Margerin<sup>22</sup>, J. B. McClean<sup>5</sup>, D. Mimoun<sup>8</sup>, N. Murdoch<sup>8</sup>, F. Nimmo<sup>23</sup>, M. Nonon<sup>14</sup>, C. Pardo<sup>2</sup>, A. Rivoldini<sup>24</sup>, J. A. Rodriguez Manfredi<sup>25</sup>, H. Samuel<sup>2</sup>, M. Schimmel<sup>26</sup>, A. E. Stott<sup>5</sup>, E. Stutzmann<sup>2</sup>, N. Teanby<sup>12</sup>, T. Warren<sup>27</sup>, R. C. Weber<sup>28</sup>, M. Wiczorek<sup>29</sup> & C. Yana<sup>14</sup>

1 Institute of Geophysics, Department of Earth Sciences, ETH Zurich, Zurich, Switzerland

2 Université de Paris, Institut de physique du globe de Paris, CNRS, F-75005 Paris, France

3 Institut Universitaire de France, 1 rue Descartes, 75005 Paris, France

4 Jet Propulsion Laboratory, California Institute of Technology, Pasadena, CA, USA

5 Department of Electrical and Electronic Engineering, Imperial College London, London, UK

6 Max Planck Institute for Solar System Research, Göttingen, Germany

7 Swiss Seismological Service (SED), ETH Zurich, Zurich, Switzerland

8 Institut Supérieur de l'Aéronautique et de l'Espace SUPAERO, Toulouse, France

9 Institute of Theoretical Physics, University of Zurich, Zurich, Switzerland.

10 Cornell Center for Astrophysics and Planetary Science, Cornell University, Ithaca, New York, USA

11 Laboratoire de Planétologie et Géodynamique, Univ. Nantes, Univ. Angers, CNRS, Nantes, France

12 School of Earth Sciences, University of Bristol, Bristol, UK

13 Laboratoire de Météorologie Dynamique, Sorbonne University, Paris, France

14 Centre National d'Etudes Spatiales, Toulouse, France

15 Institut de minéralogie, de Physique des Matériaux et de Cosmochimie, Muséum National d'Histoire Naturelle, Sorbonne University, Paris

16 Department of Earth, Environmental, and Planetary Sciences, Brown University, Providence, RI, USA

17 Schmidt Institute of Physics of the Earth, Russian Academy of Sciences, Moscow, Russia

18 Department of Geology, University of Maryland, College Park, MD, USA

19 Department of Geosciences, Virginia Polytechnic Institute, Blacksburg, VA, USA

20 DLR Institute of Planetary Research, Berlin, Germany

21 Bensberg Observatory, University of Cologne, Bergisch Gladbach, Germany

22 Institut de Recherche en Astrophysique et Planétologie, Université Toulouse III Paul Sabatier, CNRS, CNES, Toulouse, France

23 Dept. of Earth and Planetary Sciences, University of California Santa Cruz, Santa Cruz, CA, USA

24 Royal Observatory of Belgium, Brussels, Belgium

25 Centro de Astrobiología - Instituto Nacional de Técnica Aeroespacial, Madrid, Spain

26 The Institute of Earth Sciences Jaume Almera of the Spanish Scientific Research Council (ICTJA-CSIC), Barcelona, Spain

27 University of Oxford, Department of Physics, Oxford, UK

28 NASA Marshall Space Flight Center, Huntsville, AL, USA

29 Université Côte d'Azur, Observatoire de la Côte d'Azur, CNRS, Laboratoire Lagrange, Nice, France

## **SII. Wind noise and Signal to Noise Ratio (SNR) for events**

### **Noise characteristics**

All low frequency events, with the exception of events S105a, S0173a, S0167b and S0235b have amplitudes below  $10^{-9}$  m/s<sup>2</sup>/Hz<sup>1/2</sup> and moreover several events have maximum spectral amplitude less than  $3 \times 10^{-10}$  m/s<sup>2</sup>/Hz<sup>1/2</sup>. As shown and developed in Lognonné et al. (2020), these amplitudes are comparable to the wind induced lander noise. A careful noise analysis is therefore required for assessing the possible wind corruption.

The first source of noise between 0.1 and 1Hz is likely related to lander vibrations, though not resonances. While on the deck, prior to surface deployment, the SEIS-SP instrument recorded accelerations in this bandwidth between  $5 \times 10^{-8}$  and  $10^{-5}$  m/s<sup>2</sup>/Hz<sup>1/2</sup> depending on the wind and local time. These vibrations are transferred to the ground through the feet of the lander as an inertial force, producing a static deformation of the regolith and its crust, in addition to possible coupling through the tether (Murdoch et al., 2017a). Additionally, glitches provide a second source of noise in this bandwidth, owing to thermal and wind induced tilts (Lognonné et al., 2020).

The InSight TWINS wind sensors (Banfield et al., 2019) are unable to provide precise data in the same bandwidth as SEIS and have limited to no resolution for low wind. For winds below 0.7 m/s to 1.8 m/s and corresponding to Reynolds number smaller than 50, the resolution is unknown and so the data are unreliable. For a Reynolds number up to 90 (corresponding to wind speed up to 2.8 m/s for a pressure of 750 Pa), the full resolution of 0.4 m/s might in addition not be reached (Banfield et al, 2020).

Most wind data are acquired at a rate of 1 measurement every 2 seconds with the addition of some periods obtained at a rate of 1 measurement per second. No wind data are therefore available in the frequency bandwidth of the recorded events, above 0.2 Hz. Both long period and short period observations shows however a significant wind sensitivity, which is detailed in Lognonné et al. (2020), Supplementary Information SII and shows a clear increase of the noise with the mean wind.

Vertical noise levels and associated fluctuations are shown in Figure SII.1, which shows the wind levels obtained for different periods and, for a squared wind of  $10.5$  (m/s)<sup>2</sup>, the variability of all spectra. This suggest a variability of  $\pm 50\%$  of the amplitude at 1-sigma, and therefore a power spectrum SNR with respect to this source of noise of 2.25 in order to be above the 1-sigma level. Note that this variability can also lead to wind noise smaller than the average by a factor of about 2.

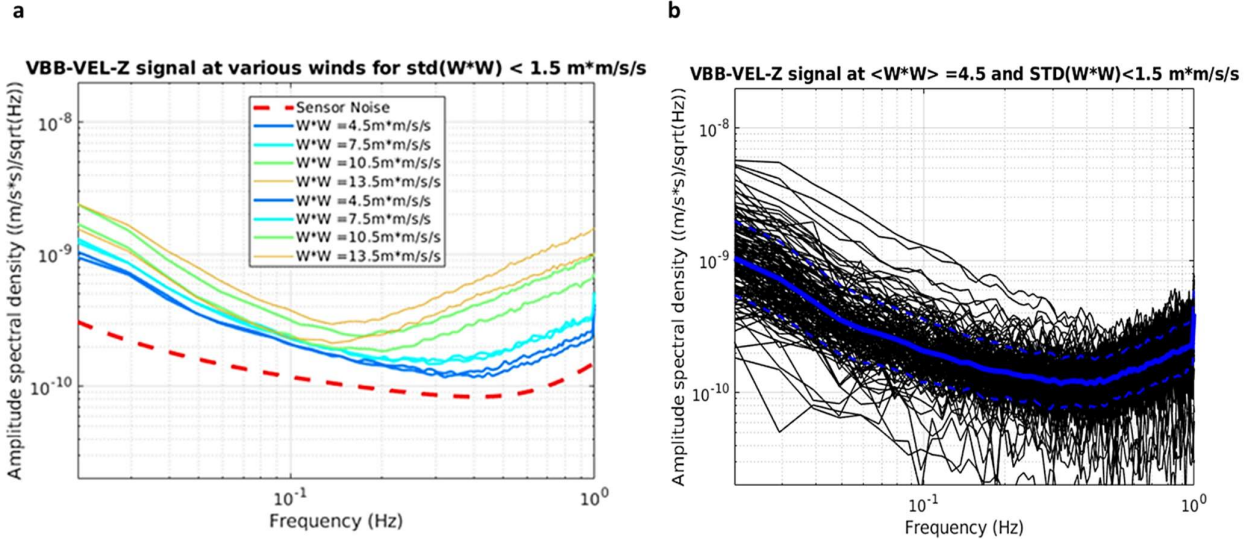


**Figure SI1.1 a**, Z axis noise for low winds (up to  $\sim 3.7$  m/s =  $13.5$  (m/s) $^2$  and standard deviation of wind-squared speed lower than  $1.5$  (m/s) $^2$ ) estimated from two sol ranges: 168-174 and 176-182. **b**, SEIS-VBBZ noise fluctuations for spectrum of 161 windows of 400 second-long in the 176-182 sols range, all taken for a same set of wind-squared (in the 3 to 6 (m/s) $^2$  range) and wind-squared standard-deviation (in the 0-1.5 (m/s) $^2$ ).

### A priori SNR from wind data

A proposed approach is to define a SNR with respect to the wind by analyzing the variations of the SEIS axis noise, as a function of the mean squared wind. We used the noise shown in Figure SI2.1 (from Lognonné et al. (2020)) to express the statistical noise level and limit the discussion to the Z axis of the VBB instrument. This noise model is approximated by the following expression for the power spectral amplitude  $n^2$ :

$$n^2 = e^2 + \left( 0.0058 \frac{\langle v^2 \rangle}{f^2} + 0.44 f^2 \langle v^2 \rangle^2 \right) 10^{-20} \text{ms}^{-2} \text{Hz}^{-1/2},$$

where  $\langle v^2 \rangle$  is the mean squared wind in (m/s) $^2$  over a given time window,  $f$  the frequency in Hz and  $e$  the VBB self-noise power for no wind. The self-noise is about 50% of the noise level for a mean squared wind of  $4.5$  (m/s) $^2$ . This expression fits to the observed noise at level better than 30% for winds up to 4 m/s, which is comparable to the noise levels observed for different sols (see Figure SI1.1).

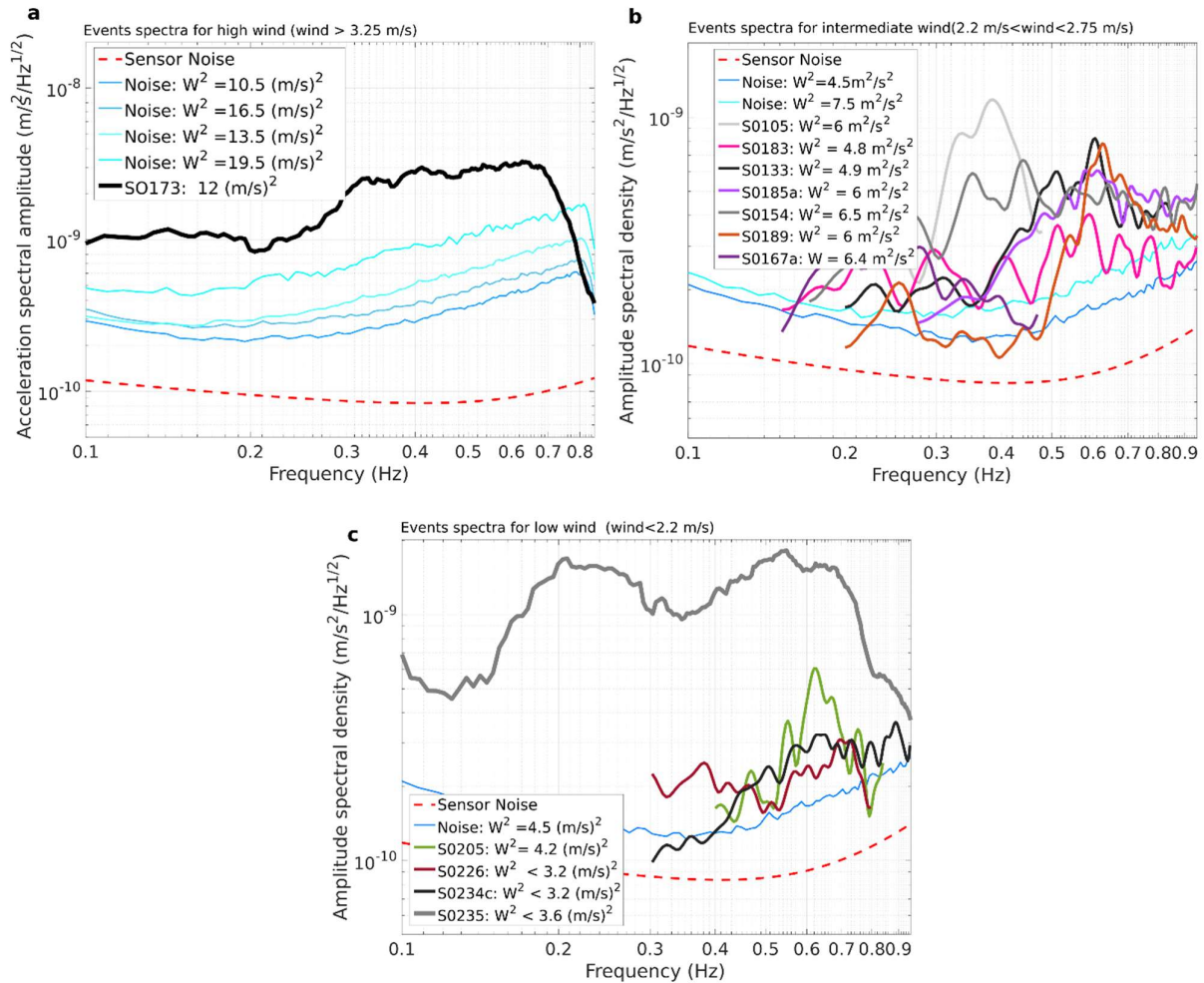


**Figure S11.2** Comparison of the events spectra with the a priori wind level for all LF events and for 3 different wind regimes. **a**, Events S0173a as compared to noise levels with wind > 3.25 m/s. **b**, Events S0105a, S0133a, S0154a, S0167a, S0185a, S0189a for noise levels with wind between 2.2 m/s and 2.75 m/s. **c**, S0205a, S0226b, S0234c and S0235b for the a priori low noise levels with winds < 2.2 m/s. For each event, the square of the mean wind in the time window used for the spectrum computation is given. The thin blue lines are the mean noise levels found for the two time windows provided in Table S11.2.

We use this wind noise to compute the a priori wind SNR, named SNRZW. It will be used to provide an initial assessment of the potential corruption of the event by wind. For an event in which energy is mostly detected between two frequencies  $f_1$  and  $f_2$ , the SNR is then simply defined as the ratio of the event's integrated PSD by the integrated energy of the above model, both integrations being done between  $f_1$  and  $f_2$ . This is practically done by using the TWINS data for computing the mean squared wind in the time window of the event. In order to address the limitation of TWINS described above for winds lower than 1.8 m/s, we use a worst-case approach and assign to all TWINS value lower than

1.8 m/s the worst-case value of 1.8 m/s. The variability of the wind is characterized by computing the maximum wind in the event window.

For events S0105, S0133a, S0154a, S0167a, S0183a, S0185a, S0189a, the average wind is intermediate and ranging from 2.0 to 2.8 m/s in the event time window, while for event S0173a, the mean wind is larger than 3.25 m/s. Wind peaks range from 3.4 to 4 m/s for all events, except S0183a, for which the maximum wind burst is 4.4 m/s. For events S0226b, S0234c, S0235b, the mean wind is low and below the 1.8 m/s limit, while the peaks range from 2.1 to 2.4 m/s, and TWINS is likely unable to resolve these low winds and only the seismic SNR shall be considered. Figure SI1.2 shows all individual spectra for these low frequency (LF) events for these three wind conditions while the SNR are given in Table SI1.1.

### **SNR from seismic only analysis (peak-to-peak and mean)**

We compute SNRs from seismic data using two approaches:

1) We use the spectral characteristics of the signal and the noise, for a direct comparison with the wind a priori: We define the spectral SNR as the ratio of spectral power during the event compared to pre-event noise spectral power. The spectral power is calculated by integrating over the power spectral density in the same frequency range described in Table SI1.1. The power spectral density is estimated using Welch's method on 50s long time windows with an overlap of 50%, separately detrended and tapered with a Hanning window. The data has been corrected for the instrument response, converted to acceleration and rotated to a ZNE coordinate system. Event windows are the same as for the a priori wind and noise windows and are available in the MQS catalogue. Results are provided in Table SI1.1 for a selection of low frequency (LF) and high frequency (HF) events for the purpose of wind contamination analysis, using a spectral window length of 40 s. The SNRs for the full list of events are in Extended Data Fig. 5.

2) We also estimate SNR values on the spectral envelopes (SEs). The SEs are computed on acceleration spectrograms for the frequency band specific to each event, using the window lengths of 40s and 60s with an overlap of 50% after instrument correction and rotation to ZNE orientation. Next, we visually check spectrograms and mask the envelope time series where there is apparent contamination from glitches (Fig. 3 in the main text). These masked portions are ignored in any analysis done using the envelopes.

We provide four measures of SNRs using envelopes: a) Amplitude ratios of maxima (peak-to-peak SNR), b) mean (mean-to-mean SNR) of signal and noise, c) P-wave envelopes SNR, and d) S-wave envelopes SNR. Maximum energy for S0183a and for S0234c is within the P-wave windows; hence, peak-to-peak and P-window SNR values for these events are equal. Similarly, all other events have same SNR values for S-wave and peak-to-peak amplitudes, as maximum energy already lies inside the

S-wave window. Table SI1.2 lists related SE amplitudes as well as the frequency bands that SNR values and SEs are computed.

### SNR from moment matching of signal energies

While the pressure and wind signals are not found to be coherent to the seismic signal to any substantial degree in the seismic bandwidth, the pressure and seismic energies are found to co-modulate with the wind speed, though with a time-dependent sensitivity (Lognonné et al., 2020 Supplementary Information 1). We use a time-dependent sensitivity from the variation of pressure energy and wind speed with seismic energy prior to an event, and hence estimate the environmental injection during the event. This is achieved by calculating the first and second moments, the mean and variance, of the pressure energy, wind speed and seismic energy within a window, and then recalculating the subsequent pressure and wind time series to match the mean and variance of the seismic time series in the window. Essentially the gain and offset of the two time series are adjusted to best match the seismic time series.

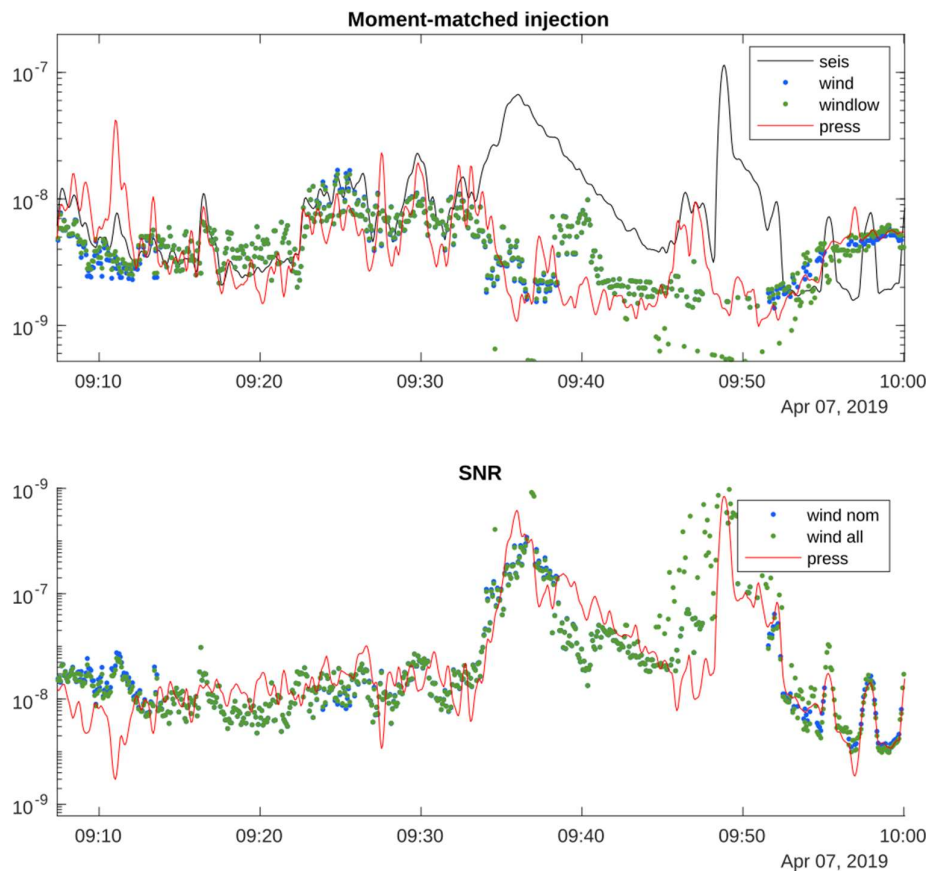


**Figure SI1.3** Environmental injection estimation using moment matching of the pressure and seismic signal energies and the wind speed for event S0128a. See text for details.

We match in the log of the signals to de-emphasise the contribution of glitches to the moment calculations and allow for power-law variation. A window length and delay of 1000s are found to produce stable results and corresponds to the typical event length. Figure SI1.3 shows the technique applied to the S0128a event, a large detected during an active period of the sol. The wind speed and pressure energies are reasonably matched to the seismic variation prior to the event, with a divergence apparent as the seismic signal rises above the environmental injection. The signals then converge briefly before a robot arm movement, from 09:48, occurs, demonstrating the ability of the technique to detect non-environmental injection. Two estimates of the wind injection are made, using all the data and masking any measurements below 2.8 m/s. There is generally good agreement between the three estimates though from 09:45 to 09:55 low wind measurements below 2.8 m/s the wind contribution diverges as anomalously low readings cause the contribution to be underestimated.

The lower plot in the figure shows the SNR derived by taking the ratio of the seismic energy to the estimates of the environmental injection. The estimates are similar apart from where low wind readings contribute. An SNR close to unity is seen prior to the event, as the moment matching normalizes the ratio, with a peak value of 1400 for pressure. SNR for all events are given in Table SI1.3.

### **Comparison of SNR measures**

Table SI1.1 shows the SNR<sub>ZW</sub> for all events analyzed in this study and the seismic SNR analysis made with a pre-event time window and the event time window, while Table SI1.2 shows the SNR from spectrogram seismic analysis. Finally, Table SI1.3 contains the SNR derived from environmental co-modulation.

The two poorer SNR<sub>WZ</sub> events are S0167a and S0189a, but they both have at least the displacement or acceleration SNR<sub>WZ</sub> larger than 2.25. The 4 best events with a SNR<sub>WZ</sub> larger than 4 (about 2-sigma away from wind fluctuations) are S0154a, S0133a, S0105a and S0173a. For the 9 events discussed, all SNR<sub>ZW</sub> except S0105a and S0173a are within -50%/+100% of the SNR obtained only from seismic data, made for two different time windows.

Figure SI1.4 shows a comparison of the SNRs from the wind injection from the a priori spectral determinations and the pressure and wind injections for the moment-matching the signals against the seismic estimate. The environmental SNR estimates are expected to be generally similar or lower than the seismic estimates at low SNRs, as environmental injection is more likely to be a significant part of the signal energy during the event. Higher environmental SNRs are seen for events when environmental injection is generally high but the event was detected during a lull, such as for S0128a, seen in Figure SI1.3. In all cases the environmental estimates reflect the SNR during the event itself, while the seismic estimates necessarily compare the event signal with a nearby quieter period.



For the lower SNR events, when validation is most critical, there is reasonable agreement between all three estimates, with an average ratio of the estimators for all SNRs below 10 being  $0.9 \pm 0.3$ .

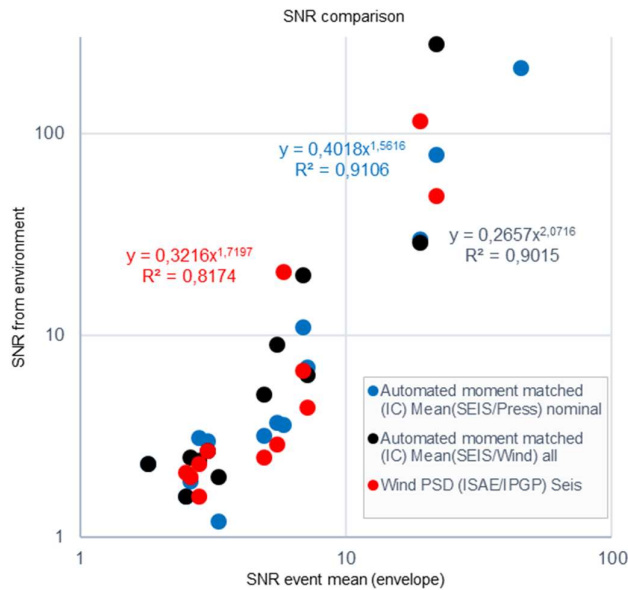


**Figure S11.4** Environmental injection estimations of the event SNR from the wind injection from the a priori spectral determinations and the pressure and wind injections for the moment-matching the signals against the seismic estimates.

### SNR application to S0189a event

*SNR from wind data:* Figure S11.5 demonstrates the significance of the seismic signal, comparing spectra from the vertical component of the VBB sensor for the event (red) and pre-event background noise (green). Also shown are background spectra for all other times with similar winds (black) and the mean (solid blue) and standard deviation (dashed blue). The event has a clearly anomalously high amplitude peaking far above the 1-sigma level especially for frequencies above 0.45 Hz, and the background seismic noise is lower than normal. The event has a power signal to noise ratio of 2.5 with respect to these a-priori wind generated noise amplitudes.

*SNR from seismic only analysis:* this event has signal-to-noise ratios of 10.3, 4.9, 4.3 and 10.3 using peak-to-peak, mean-to-mean, peak P wave and peak S wave amplitudes of spectral envelopes, respectively.

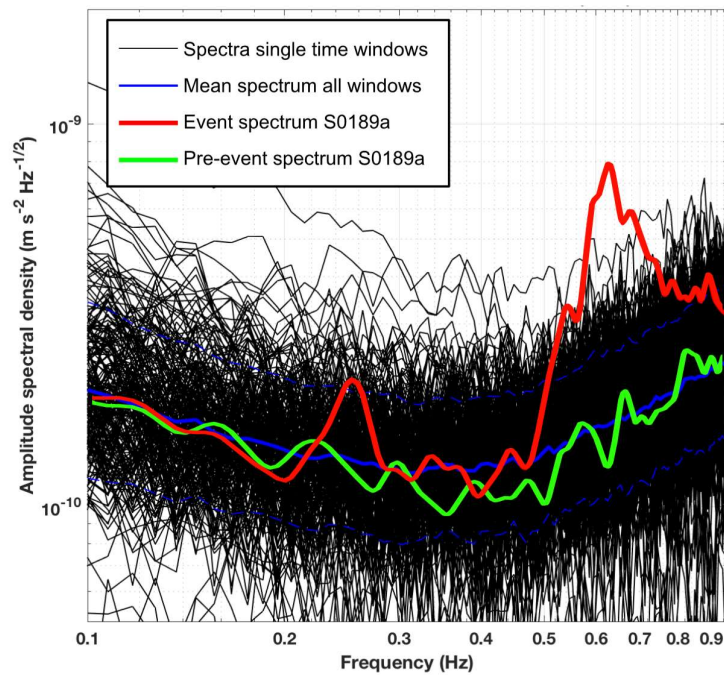


**Figure S11.5** Amplitude spectral density (ASD) of vertical VBB component for the event on Sol 189 (red) compared to ASDs from time windows that have similar wind speed to that recorded during the event (black lines). The blue solid line shows the median ASD of all those time windows. During the event, the squared wind speed was  $7(\text{m/s})^2$ . The green line is the ASD directly before the event, showing that the noise before the event was quite close to the median observed for a squared wind of  $6(\text{m/s})^2$ . The event red spectrum is far above the 1-sigma fluctuations (dashed blue lines).

*SNR from moment matching of signal energies:* Figure S11.6 compares temporal changes in wind and pressure with the amplitudes of the observed seismic signal. This allows assessment of the contribution from the local environment in the seismic signal during an event and can be quantified by matching the first two moments, mean and variance, of the pressure and seismic energy in the event bandwidth to the wind speed. The matching is done by estimating the statistical moments over a lagging time window, to avoid matching the statistics during the event. In this analysis, a potential event can be considered of a seismic rather than environmental origin if the seismic signal diverges from the expected match of the two environmental injections. In Figure S11.6 the seismic energy diverges from the tracked temporal changes in the environmental signals, indicating that the signal source is not due to environmental injection. The seismic energy during the event is significantly above the environmental injection, validating a non-local source for the seismic signal. The wind is shown to vary throughout with a weak periodicity and an aseismic increase in the pressure energy is seen at 05:27 UTC, before the event's arrival. A few locally-generated spikes of energy, or glitches, can also be seen in the seismic signal, dominantly in the East and North components.

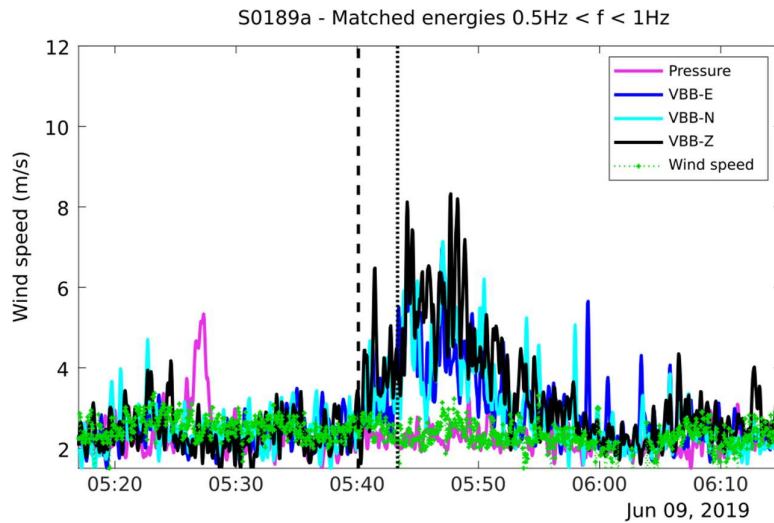


**Figure S11.6** Matched energy summary for the S0189a seismic event. The matched energies for the 3 components of VBB acceleration and pressure are compared to the wind speed. Before and after the event, the VBB acceleration energies in each of the three VBB components follow the same temporal changes in the wind speed, which itself exhibits a weak periodicity in the duration shown. P- and S-wave picks are shown by the vertical black dashed and dotted lines. The seismic event is seen to diverge above the environmental contributions at the time of the P-wave pick.

**Table S11.1** SNR related to wind (SNRZW), as well as mean squared wind, maximum wind in the event window and Seismic SNR for all LF events. SNRZW are either given in displacement or acceleration. All wind squared STD are in the range of 1.3-1.8 (m/s)<sup>2</sup>, with the exception of S0173 and S0205a for which more stable winds are observed with STD < 0.8 (m/s)<sup>2</sup>. Values in bold are those above the 2.8 m/s level, for which TWINS has its full resolution. Value in red are those below the 1.8 m/s TWINS resolution threshold. Seismic SNR from acceleration power spectra uses the same frequency range on instrument corrected waveforms.

Event name	Mean Wind	Wind std <sup>2</sup>	Wind max	SNRZW	SNRZW
	(m/s)	(m/s) <sup>2</sup>	(m/s)	(Displacement)	(Acceleration)
S0105a (Z)	2.43	1.28	<b>3.36</b>	24.4	21.0
S0133a (Z)	2.07	1.8	<b>3.67</b>	5.8	8.2
S0154a (Z)	2.53	1.85	<b>3.8</b>	3.8	4.4
S0167a (Z)	2.52	1.63	<b>3.95</b>	2.5	1.6
S0173a (Z)	<b>3.47</b>	0.88	<b>4.00</b>	104	116.1
S0183a (Z)	2.19	1.38	<b>4.38</b>	2.2	2.3
S0185a (Z)	2.29	1.82	<b>3.66</b>	2.7	3.7
S0189a (Z)	2.44	1.55	<b>3.53</b>	1.7	2.5
S0205a (Z)	2	0.71	2.11	2.6	2.8
S0226b (Z)	<b>1.3</b>	<b>1.28</b>	<b>2.40</b>	<b>5</b>	<b>4.5</b>
S0234c (Z)	<b>1.87</b>	<b>0.42</b>	<b>2.25</b>	<b>1.8</b>	<b>2.2</b>
S0235b (Z)	<b>0.75</b>	<b>0.92</b>	<b>2.11</b>	<b>78.6</b>	<b>148.8</b>

**Table SII.2** SNR derived from spectral envelopes and acceleration spectra for a selection of HF and LF events. The seismic component used for measuring envelope amplitudes are indicated in parenthesis next to the event names. Signal amplitudes are measured in the envelope time series between signal start and end for the listed frequency range specific to each event, after contamination from glitches are masked. Noise is assumed to be the remaining part of the envelope data.

Event name	SNRs from spectral density envelopes (acceleration)				Signal start (UTC)	Signal end (UTC)	f <sub>min</sub> (Hz)	f <sub>max</sub> (Hz)
	Peak signal / peak noise	Mean signal / mean noise	max(P) / peak noise	max(S) / peak noise				
S0105a (Z)	6,8	5,8	4,4	6,8	2019-03-14 20:53:28	2019-03-14 21:28:36	0.31	0.5
S0133a (Z)	11,4	6,9		11,4	2019-04-12 18:04:34	2019-04-12 18:38:48	0.33	0.67
S0154a (Z)	7,9	7,1		7,9	2019-05-04 06:57:28	2019-05-04 07:37:48	0.17	0.67
S0167a (Z)	3,8	2,8		3,8	2019-05-17 16:37:20	2019-05-17 17:13:06	0.18	0.48
S0173a (Z)	94	18,9	35,1	94	2019-05-23 02:12:58	2019-05-23 03:09:54	0.2	0.67
S0183a (Z)	7,5	2,8	7,5	1,9	2019-06-03 02:17:47	2019-06-03 02:48:54	0.33	0.66
S0185a (Z)	14,8	5,5	5,2	14,8	2019-06-05 02:03:25	2019-06-05 02:49:55	0.28	0.83
S0189a (Z)	10,3	4,9	4,3	10,3	2019-06-09 05:30:05	2019-06-09 06:07:57	0.36	0.83
S0205a (Z)	4,5	3	4,5		2019-06-25 16:59:43	2019-06-25 17:26:14	0.29	0.83
S0226b (Z)	5,6	2,6		5,6	2019-07-17 05:33:38	2019-07-17 06:12:49	0.33	0.83
S0234c (Z)	4	2,5	1,6	4	2019-07-25 12:44:18	2019-07-25 13:19:32	0.33	0.83
S0235b (Z)	227,8	21,8	28	227,8	2019-07-26 12:09:16	2019-07-26 13:28:08	0.15	0.91
<i>High frequency events</i>								
S0128a (N)	122,7	45,4		122,7	2019-04-07 09:23:36	2019-04-07 09:55:55	3	7.5
S0218a (N)	9,7	3,3		9,7	2019-07-09 04:53:00	2019-07-09 05:34:45	5	7.5
S0226a (N)	2,3	1,8		2,3	2019-07-17 04:24:18	2019-07-17 04:49:18	3	7.5
S0239a (N)	2,5	2		2,5	2019-07-30 14:16:49	2019-07-30 14:29:52	3	5

**Table SII.3** SNR from moment matching of signal energies.

Event name	Automated moment matched (IC)					
	Peak (SEIS/Press)	Peak (SEIS/Wind)		Mean (SEIS/Press)	Mean (SEIS/Wind)	
		Nominal	All		Nominal	All
S0105a (Z)	14	10		3.6	3.3	
S0133a (Z)	<b>31</b>	<b>10</b>	144	<b>11</b>	<b>7.3</b>	20
S0154a (Z)	16	9	17	7	8	6.4
S0167a (Z)						
S0173a (Z)	170	160	160	30	29	29
S0183a (Z)	17		12	3.1		2.4
S0185a (Z)	40		70	3.7	4.6	9
S0189a (Z)	7.4	9.7	13	3.2	4.7	5.1
S0205a (Z)	12		7	3		2.7
S0226b (Z)	3.9		3.9	1.9		2.5
S0234c (Z)	3.1		3.1	1.6		1.6
S0235b (Z)	670		3500	79		280
<i>High frequency events</i>						
S0128a (N)	3400	1400	2.8E+05	214	84	1900
S0218a (N)	2.9	6.5	7.8	1.2	2.1	2
S0226a (N)	4.5		5.3	2.3		2.3

## **SI2. Interior structure models**

The following sections briefly describe how the interior structure models that are used by MQS for locating marsquakes are constructed and how they were used in the location of marsquakes.

The main method for the latter has been described in previous articles (Böse et al., 2016; Khan et al., 2016).

In all, we used 2500 models and to ensure sufficient coverage of the a priori model space, three independent groups from different institutions were solicited for models. Generally, all models were constructed so as to satisfy current observations of mass, moment of inertia, and tidal response. A particular effort was spent on deriving models using different methodologies (thermal history modeling and inversion) and a variety of starting bulk Mars compositions following the approaches detailed in Khan et al. (2018), Rivoldini et al. (2011), Samuel et al. (2019).

Initially, many more models have been considered, but testing showed little difference in resulting marsquake locations, and for the purpose of providing a location in a foreseeable time (on the order of minutes), the initial larger series of models were down-selected to the current set of 2500 models. The current set of models span a relatively large range as shown in Figure SI2.1 and encompasses, among others, all earlier literature models (see eg. Smrekar et al., 2019 for a review) and, consequently, are expected to cover the plausible range of Martian models within which the “true” model lies. While this is a reasonable working hypothesis, we nonetheless constantly strive to update and extend the database with models that derive from novel experimental data, methods, and InSight seismic data (Panning et al., 2016). In the following, we briefly describe the main modeling methods and the down-selection procedure and refer the reader for more details to the various studies.

### **Geodetically-constrained models**

The models described in the following are mainly detailed in Rivoldini et al. (2011). The models are spherical, isotropic, non-rotating, and in hydrostatic equilibrium. We assume a convecting and fully liquid iron-sulfur core overlain by a solid silicate mantle and crust. The depth dependent elastic properties of the iron-sulfur alloy in the core are computed following Dumberry & Rivoldini (2015). For the mantle, we consider 5 different compositions (Lodders & Fegley, 1997; Mohapatra & Murty, 2003; Sanloup et al., 1999; Taylor, 2013; Brasser et al., 2018) deduced from the analysis of Martian meteorites. The thermal state of the mantle in our models is bounded by two end-member (“hottest” and “coldest” profiles) temperature profiles obtained from the thermal evolution study of Plesa et al. (2016). The elastic properties of the mantle are calculated with *Perple\_X* (Connolly, 2009) using the thermodynamic formulation of Stixrude and Lithgow-Bertelloni (2005) and parameters of Stixrude and Lithgow-Bertelloni (2011). For the crust, we use two basaltic chemical compositions (Babeyko &

Zharkov, 2000; Khan et al., 2018) either pure or mechanically mixed with a variable amount of periclase. The elastic properties of the basaltic end-members and periclase phase are computed similarly to those of the mantle. To take into account the presence of a low density bed-rock layer and the crustal porosity we amend the computed elastic properties with a pressure dependent function (Khan et al., 2018) that allows for an increase in density from bed-rock at the surface to porosity free material at depth. The closing depth of the porosity and the amount of periclase are chosen such that the average crustal density is in agreement with Wieczorek & Zuber (2004). For the shear attenuation of the silicate shell at 1 s we use PREM (Dziewonski & Anderson, 1981) values at equivalent pressure, i.e., 600 and 140 in the crust and mantle, respectively. Finally, following Rivoldini et al. (2011), the models agree with the observed mass of the planet and to within 3 sigma of the observed moment of inertia value of  $0.3638 \pm 0.0003$  (Konopliv et al., 2016).

### **Geophysically-constrained models**

The models described in the following are obtained from inversion of the most recent set of geophysical data, including mean density ( $3.9350 \pm 0.0012 \text{ g/cm}^3$ ), mean moment of inertia ( $0.36379 \pm 0.0001$ ), and tidal response ( $k_2 = 0.169 \pm 0.006$  and  $Q = 95 \pm 10$ ) as described in Khan et al. (2018). Briefly, a set of Martian compositions (Dreibus & Wänke, 1984; Lodders & Fegley, 1997; Sanloup et al., 1999; Taylor, 2013) are explored in the  $\text{NaO}_2\text{-CaO-FeO-MgO-Al}_2\text{O}_3\text{-SiO}_2$  model chemical system; a chemical model which accounts for >98% of the mass of the Martian mantle (Dreibus & Wänke, 1984; Bertka and Fei, 1997). Here, Martian mineralogy and physical properties are assumed to be governed by thermodynamic equilibrium and computed for a given model pressure, temperature, and bulk composition along self-consistent adiabats by Gibbs free-energy minimization (Connolly, 2009) using the thermodynamic formulation and parameters of Stixrude & Lithgow-Bertelloni (2005, 2011). The core is assumed to consist of a binary mixture of Fe-S, which is entirely liquid, well-mixed, and convecting. Following the parameterisation of Rivoldini et al. (2011), thermoelastic properties for the core are computed using equations-of-state for liquid iron and liquid iron-sulfur alloys. The crust is likely to be more complex lithologically, not equilibrated, and is probably porous. The effect of porosity is taken into account by assuming porosity ( $f$ ) to decrease linearly from <1 at the surface to 0 at the Moho through a decrease in crustal seismic velocity and density by multiplying  $(1-f)$  with either seismic property, while crustal composition is fixed to that of Taylor and Maclennan (2009). Shear attenuation and velocity profiles are computed using the laboratory-based grain size- and frequency-dependent viscoelastic model of Jackson & Faul (2010), from which frequency-dependent tidal response functions can be computed. Shear attenuation in the crust and lithosphere is fixed to 600 after PREM (Dziewonski and Anderson, 1981). As for the core, we assume that dissipation only occurs in shear.

## Thermal evolution models

The models described in the following are detailed in Samuel et al. (2019). A suite of geodynamically-constrained models was built from running the equivalent of 4.5 Gyr of thermo-chemical evolution of a Mars-like planet. The latter was composed of an adiabatic liquid iron alloy core (with the light element assumed to be sulfur, see Rivoldini et al. (2011), surrounded by a silicate envelope. The silicate envelope consisted of an adiabatic mantle convecting under a stagnant i.e., essentially diffusive) lithospheric lid, the thickness of which including that of a crust enriched in heat-producing elements, evolves with time. The thermo-chemical evolution was computed using a parameterized approach (e.g. Breuer & Spohn, 2006; Hauck & Philipps, 2002) and includes temperature and pressure-dependent mantle viscosity (Samuel et al., 2019; Thiriet et al., 2018) and references therein). By systematically varying six governing parameters within plausible ranges, a collection of thermal profiles was obtained. The parameters are effective activation energy of the mantle, activation volume, reference viscosity, initial mantle temperature under the lithospheric lid, initial core temperature at the core-mantle boundary (CMB), and core radius. The values of all other physical parameters are listed in Samuel et al. (2019) (Table S1.3), with the exception of average mantle and core density, thermal expansion, and specific heat, which were obtained through the successive application of the thermal evolution and the mineral physics model. Cases for which the convective mantle went sub-critical were excluded.

In the crust, body wave velocities and density were assumed to be constant. Crustal density and core sulfur content were varied via bisection to ensure that models satisfy mass and moment of inertia constraints within uncertainties. The uppermost part of the crust consisted of a fixed 2-km-thick bedrock layer with a reduced density and seismic velocities. The geodynamically-computed present-day areotherms were used to determine mantle densities and seismic velocities with `Perple_X` (Connolly, 2009) using the thermodynamic formulation of Stixrude & Lithgow-Bertelloni (2005) and parameters of Stixrude & Lithgow-Bertelloni (2011) for the bulk mantle composition of Taylor et al. (2006). Finally, only models with degree-two Love number values (that include both elastic and anelastic contributions, computed following the approach described in Khan et al., 2004) located within the 3-sigma range of the currently observed value  $0.169 \pm 0.018$  (Konopliv et al., 2016), were retained.

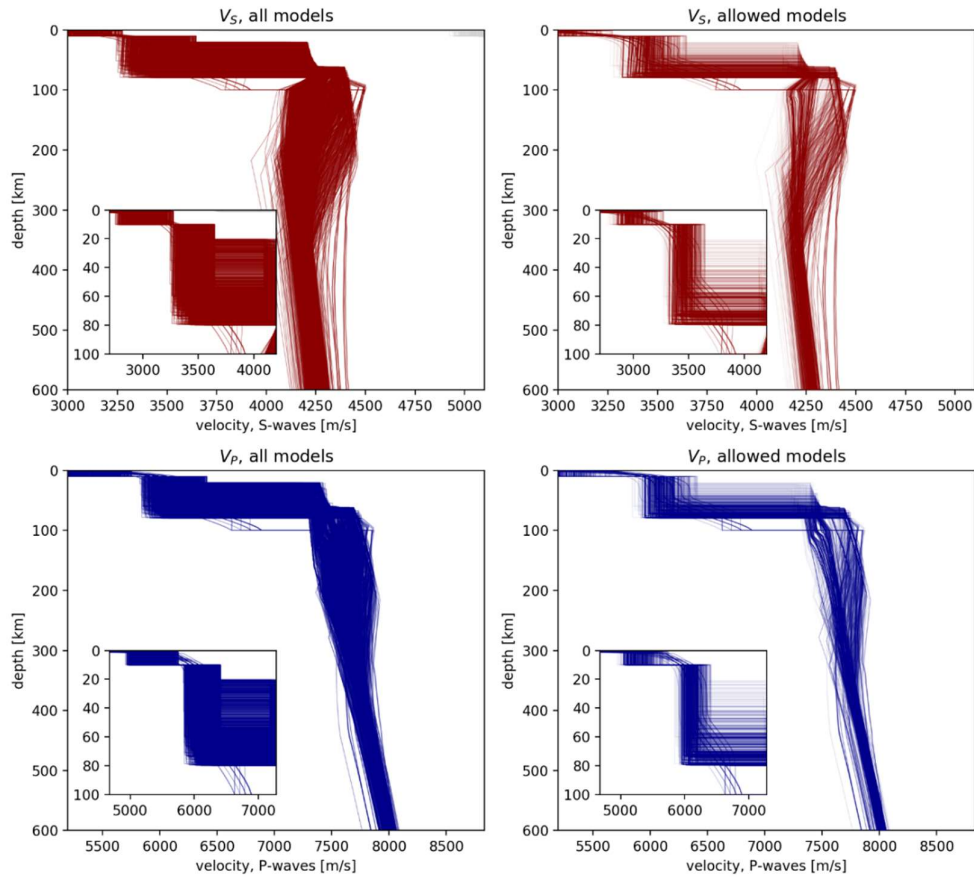


**Figure SI2.1** A priori S- and P-wave models used for location of events (left), compared with models compatible with S-P travel time differences of  $174 \pm 3$  s (S0173a) and  $157 \pm 4$  s (S0235b) (right). The extensive S-wave shadow zone in 20-60 degree epicentral distance predicted by many of the a priori models is not compatible with these observations. The allowed models have relatively thick crusts (60-80 km) and a velocity increase or only slight decrease directly below the Moho.

### Model down-selection using seismic observations

For locating marsquakes, we perform a grid search over all possible depths, distances, and prior models (Böse et al., 2017; Khan et al., 2016). Measured arrival times relative to an identified P phase are compared to pre-calculated travel times for each combination of depth, distance, and model. Because at most two phases (P and S) corresponding to a single P-S travel time have been identified in the current set of events, interior structure cannot be constrained beyond the prior model range. The events S0235b and S0173a are fortuitous, since they occurred in an epicentral distance range of 26-30 degrees, where many a priori models predict a S-wave shadow zone. The observed P-S arrival time differences of  $174 \pm 3$  seconds (S0173a) and  $157 \pm 4$  seconds (S0235b) therefore allows us to discard 60% of the a priori models (Fig. SI2.1).



### SI3. Source characteristics: magnitude and seismic moment, spectral shape

#### Magnitudes

Magnitude estimates for the 36 low-frequency (LF) and high-frequency (HF) events in the Extended Data Fig. 4, as well as Table SI3.1 are computed using a modified formulation of that proposed by Böse *et al.* (2018), which calibrated magnitude scales for Mars by simulating the seismic wave propagation through a set of 13 representative 1D Mars models. These scales incorporated pre-mission knowledge on Mars interior structure (Smrekar *et al.*, 2019) and the ambient and instrumental noise that were expected pre-launch (Murdoch *et al.*, 2015a,b; Mimoun *et al.*, 2017). The preliminary seismic data collected by InSight suggest that (1) seismic events on Mars are observable mainly in the frequency band from 2 to 6 s, (2) in some events the arrival of separate energy packets could be interpreted as P- and S-body wave trains, while neither secondary seismic phases nor surface waves could yet be identified, and (3) a class of high-frequency events exists that are mainly visible as an increased excitation of the 2.4 Hz mode. We therefore adapted the Böse *et al.* (2018) method and used 4 different ways of estimating the moment magnitude, depending on event type. All use the epicentral distances,  $\Delta$ , derived from the travel-time alignment (see main text) for LF events, and derived from Pg-Sg travel time for HF events (with an assumed  $v_p = \sqrt{3}v_s = 4$  km/s). The amplitudes were measured depending on the magnitude type:

1. Spectral magnitude  $M_{\text{FB}}^{\text{Ma}}$ : from spectral amplitude,  $A_\theta$ , which we determined from the plateau of the displacement spectra (Figure 6);
2. Body-wave magnitudes  $m_b^{\text{Ma}}$  and  $m_{\text{bS}}^{\text{Ma}}$ : from the maximum displacement amplitude,  $A_p$  or  $A_s$ , which we determined in the time window of P- or S-arrivals from the seismograms filtered between 0.2 and 0.5 Hz;
3. 2.4Hz magnitude  $M_{2.4\text{Hz}}^{\text{Ma}}$ : from the maximum value of the 2.4 Hz amplification peak, which we determined from fitting a Lorenz curve to the displacement spectrum between 2 and 3 Hz.

All magnitudes are calibrated to give a direct estimate of the moment magnitude. For the recalibration of the magnitude scales in Böse *et al.* (2018) we assume a volumetric seismic wave propagation for the LF and a near surface propagation for the HF events. We therefore model the decay of seismic amplitudes for these two groups as 0.9 and 1.1, respectively. These values combine the effects of intrinsic attenuation, geometrical spreading and other propagation effects, and are consistent with the findings in Böse *et al.* (2018). We consider the spectral magnitude  $M_{\text{FB}}^{\text{Ma}}$  to be most reliable and use it as a reference for calibrating the other three scales using events with overlapping amplitude measurements. Details on the procedure and scales will be described in a forthcoming publication. Results for the events described in this paper are shown in Table S5.1.

## Spectral estimation

To estimate  $A_0$  for the spectral magnitude and to test whether the events are compatible with tectonic sources, a fit was made using a combination of a Brune source and an attenuation term:

$$A(f) = A_0 A_{\text{src}}(f) A_{\text{att}}(f)$$

The Brune source was estimated (following Brune, 1970) by

$$A_{\text{src}}(f) = \frac{1}{1 + (f/f_c)^2}$$

with the corner frequency  $f_c$

$$f_c = 0.49\beta(\sigma/M_0)^{1/3}$$

estimated from the moment magnitudes in Table S5.1, shear wave velocity  $\beta=3$  km/s and a stress drop  $\sigma=1$  MPa. A cursory look at the amplitudes shows that the event's moment magnitudes are below 4, so the expected corner frequency is above 1 Hz for all of the events, and the spectral shape is mainly controlled by attenuation, described by an attenuation term  $A_{\text{att}}(f) = \exp(-\pi f T/Q_{\text{eff}})$ , where  $T$  is the estimated travel time of the S-wave and  $Q_{\text{eff}}$  is an effective quality factor used to explain the spectral shape. The parameters  $Q_{\text{eff}}$  and  $A_0$  were modified to fit the recorded spectra, while the values for  $T$  and  $M_0$  were taken from the aligned distances.

The event spectra are estimated by Welch's method using time windows during the event, compared to noise windows before. The spectra were calculated in Hanning windows of 51.2 seconds length and 50% overlap. Each window was detrended linearly and zero padded by a factor of 4. Spectra were calculated on instrument-corrected and rotated data separately for all components in the ZNE coordinate system. The instrument correction was done to velocity on time windows of two hours to avoid windowing effects in the spectrum estimation. The spectra of the two horizontal channels were averaged. Displacement spectra were calculated by dividing the velocity spectrum by an array containing circular frequencies.

The biggest caveats here are instrument glitches, which are relatively common during the evening period when most events occurred, and create long-period artifacts in the estimated spectrum. Therefore, for each event, a time window is selected in which no glitches are present with a minimum length of five minutes. Additionally, a noise time window is selected before the event, again avoiding glitches and obvious atmospheric disturbances. For some events, the atmospheric situation before the event was such that no time window could be found. In this case, a time window after the event was selected with a time difference of at least thirty minutes to make sure that only noise was recorded. The exact time windows are shown in Table SI3.1.

The effective quality factor  $Q_{\text{eff}}$  was estimated manually using the same value for all events in the same distance bin. For the bin around  $27^\circ$  distance, containing the largest events (S0173a, S0235b),  $Q_{\text{eff}}$  was estimated to be  $350 \pm 50$ .

**Table SI3.1** Body-wave magnitudes,  $m_b^{\text{Ma}}$  and  $m_{\text{bS}}^{\text{Ma}}$ , 2.4Hz magnitude,  $M_{2.4\text{Hz}}^{\text{Ma}}$ , and spectral magnitude,  $M_{\text{FB}}^{\text{Ma}}$ , of all events described in the main text. Preferred magnitude is highlighted in bold. Last four columns show time windows used for spectral computations used to produce Figure 5.

Event name	$m_b^{\text{Ma}}$	$m_{\text{bS}}^{\text{Ma}}$	$M_{2.4\text{Hz}}^{\text{Ma}}$	$M_{\text{FB}}^{\text{Ma}}$	Start signal window (UTC)	End signal window (UTC)	Start noise window (UTC)	End noise window (UTC)
LF events								
S0105a	3.0	3.0	-	<b>3.2</b>				
S0133a	3.4	3.1	-	<b>3.2</b>				
S0154a	3.6	3.6	-	<b>3.5</b>	2019-05-04T07:11:49	2019-05-04T07:14:42	2019-05-04T07:38:19	2019-05-04T07:50:31
S0167a	3.5	3.7	-	<b>3.8</b>	2019-05-17T16:52:27	2019-05-17T16:58:05	2019-05-17T16:38:37	2019-05-17T16:46:20
S0173a	3.6	3.5	-	<b>3.6</b>	2019-05-23T02:25:51	2019-05-23T02:27:55	2019-05-23T01:54:16	2019-05-23T02:05:17
S0183a	3.3	3.2	-	<b>3.1</b>	2019-06-03T02:32:11	2019-06-03T02:34:08	2019-06-03T02:08:07	2019-06-03T02:16:54
S0185a	2.9	3.4	-	<b>3.1</b>	2019-06-05T02:20:48	2019-06-05T02:22:45	2019-06-05T03:06:49	2019-06-05T03:17:31
S0189a	2.5	2.7	-	<b>3.0</b>				
S0205a	2.8	3.0	-	<b>3.0</b>	2019-06-25T17:09:28	2019-06-25T17:10:53	2019-06-25T17:02:47	2019-06-25T17:08:22
S0226b	-	-	-	-	2019-07-17T05:48:44	2019-07-17T05:52:35	2019-07-17T05:21:45	2019-07-17T05:30:04
S0234c	3.2	3.2	-	<b>2.8</b>	2019-07-25T12:54:18	2019-07-25T13:09:32	2019-07-25T12:50:00	2019-07-25T12:52:58
S0235b	3.2	3.6	-	<b>3.6</b>	2019-07-26T12:21:56	2019-07-26T12:25:51	2019-07-26T12:14:20	2019-07-26T12:18:41
S0325a	3.7	3.7	-	<b>3.7</b>	2019-10-26T07:02:57	2019-10-26T07:07:13	2019-10-26T06:55:38	2019-10-26T06:58:39
HF events								
S0128a	-	-	1.9	<b>2.1</b>	2019-04-07T09:35:05	2019-04-07T09:37:35	2019-04-07T09:10:57	2019-04-07T09:18:33
S0185b	-	-	1.7	<b>2.0</b>				
S0202b	-	-	1.5	<b>1.8</b>				
S0202c	-	-	1.8	<b>1.9</b>				
S0218a	-	-	2.0	<b>2.3</b>	2019-07-09T05:08:43	2019-07-09T05:11:51	2019-07-09T04:49:44	2019-07-09T05:00:49
S0222a	-	-	<b>1.6</b>	-				
S0226a	-	-	1.2	<b>1.5</b>				
S0228c	-	-	1.7	<b>1.9</b>				
S0229a	-	-	<b>1.6</b>	-				
S0231b	-	-	1.7	<b>1.9</b>				
S0234b	-	-	1.3	-				
S0239a	-	-	1.8	<b>1.9</b>	2019-07-30T14:22:39	2019-07-30T14:24:19	2019-07-30T14:38:51	2019-07-30T14:50:49
S0246a	-	-	1.7	<b>1.8</b>				
S0257a	-	-	<b>1.8</b>	-				
S0257b	-	-	<b>1.7</b>	-				
S0260a	-	-	2.0	<b>2.2</b>	2019-08-21T05:15:52	2019-08-21T05:18:22	2019-08-21T04:48:41	2019-08-21T05:00:05
S0262b	-	-	1.7	<b>2.2</b>				
S0263a	-	-	1.4	<b>1.9</b>	2019-08-23T11:11:03	2019-08-23T11:12:58	2019-08-23T11:07:27	2019-08-23T11:09:39
S0264e	-	-	2.1	<b>2.2</b>	2019-08-25T10:37:52	2019-08-25T10:43:04	2019-08-25T09:56:07	2019-08-25T10:06:54
S0289a	-	-	2.0	<b>2.3</b>				
S0290a	-	-	<b>1.6</b>	-				
S0291c	-	-	1.7	<b>2.0</b>				
S0292a	-	-	1.8	<b>1.9</b>				

## SI4. Potential volcano-tectonic sources for quakes around InSight

Mars was tectonically active mostly prior 3 Ga (e.g., Golombek and Phillips, 2009), mainly governed by intense volcanic activity associated with extensive surface faulting. While the current tectonic activity on Mars seems negligible, “younger” fault-like structures (initiation age < 2Ma), possibly linked to recent volcanic activities (e.g. Neukum et al., 2004; Vaucher et al., 2009) represent potential sources of marsquakes.

Major geological features are well observed at the surface of Mars from orbital data (MRO, MeX, MGS, Odyssey). We show on Figure SI4.1 the main tectonic/volcanic structures in an area covering up to 70° epicentral distance from the InSight lander, where most of the quakes are located (see main text and Supplement S1). Note that we focus mainly on major extensive structures that correspond to large crustal features mostly associated with deeper processes. We thus do not describe small and surficial reverse faulting scattered over the globe (black lines on Figure SI4.1).

The closest (10° to 40° distance) and largest structure near InSight is Elysium Mons (see Figure SI4.1), a volcanic bulge associated with large dike-induced grabens situated near its apex (see Figure SI4.1) and on its southeastern flank (Cerberus Fossae and Grjótá Valles). Based on boulders and landslide distributions along the fossae, Roberts et al. (2012) and Brown & Roberts (2019) have shown that those large structures might have experienced several marsquakes in the past. Assuming that the Cerberus Fossae system is currently active (Taylor et al., 2013) and that its direction of long-term propagation is toward the East, the source of quakes would preferably be located on the eastern part of the system, where fossae are supposedly younger (i.e. propagating fault/dike tip), and thus hosting higher stress concentrations (see Green et al., 2015; Rubin & Gillard, 1998; Sigmundsson et al., 2015 for terrestrial examples).

Provided that these dike systems are active and genetically linked to Elysium Mons, quakes and tremors may be triggered by volcanic activity, which is supported by crater counting and relative stratigraphy with recent possible activity as recent as 2.5-3 Myr (Vaucher et al., 2009). A secondary vent is also observed in the North (Hecates Tholus) with normal faults and grabens (Galaxias Fossae).

At greater distance (> 40°), we identify several other structures that might be responsible for quakes (Figure SI4.1): i) the large Nili Fossae in the West, at the edge of the Isidis basin formed by impact more than 3 Ga ago (Greeley and Guest, 1987), which could still present surface instabilities leading to landslides or rockfalls; ii) in the East, the Tharsis Bulge is associated to far-field faults and overflow systems of Sirenum, Memnonia or Mangala Fossae, where late geological activity can be expected (Anderson et al., 2019); iii) the Hellas Basin region in the Southwest, where possible slope destabilizations of the basin rims might occur. Furthermore, the large regional gravity anomaly in the vicinity of Hellas could possibly be responsible for quakes, as relaxation of ancient stress field might

occur due to a significant change in the crustal thickness (from 60 km in Noachis Terra to 10-15 km in Hellas Planitia; Genova et al., 2016), associated with crustal lateral heterogeneities.

Finally, the Martian crustal dichotomy could be at the origin of local landslides and slope destabilizations (e.g., Lefort et al., 2015), with the Southern highland terrains situated 1-3km higher in elevation than the Northern lowlands, and with possibly large crustal thickness variations from  $55\pm 20$  km in the South to 32 km in the North (according to Zuber et al., 2000).

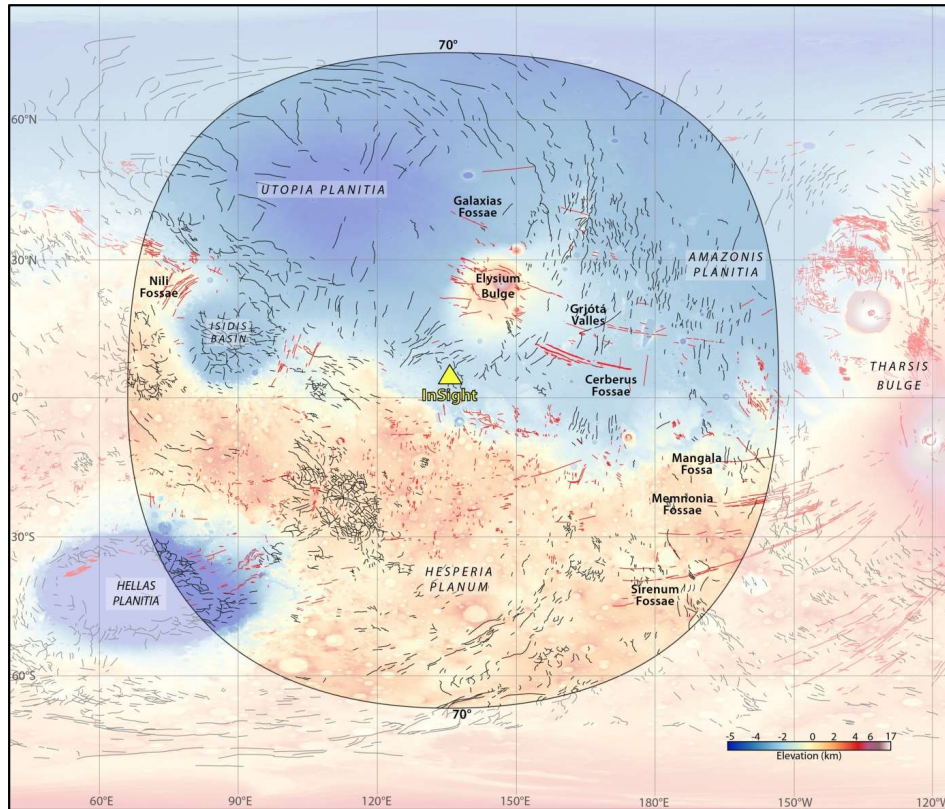


**Figure SI4.1** Regional fault map of Mars and main potential sources of quakes in a  $70^\circ$  epicentral distance range from the InSight lander (yellow triangle). The global fault map is modified from the compilation of Knapmeyer et al., 2006. Black lines represent reverse/strike slip faults and red lines are normal faults.

## References

- Anderson, R. C., Dohm, J. M., Williams, J. P., Robbins, S. J., Siwabessy, A., Golombek, M. P., & Schroeder, J. F. (2019). Unraveling the geologic and tectonic history of the Memnonia-Sirenum region of Mars: Implications on the early formation of the Tharsis rise. *Icarus*. <https://doi.org/10.1016/j.icarus.2019.06.010>
- Babeyko, A. Y., & Zharkov, V. N. (2000). Martian crust: a modeling approach. *Physics of the Earth and Planetary Interiors*, *117*(1–4), 421–435. [https://doi.org/10.1016/S0031-9201\(99\)00111-9](https://doi.org/10.1016/S0031-9201(99)00111-9)
- Banfield, D., Rodriguez-Manfredi, J.A., Russell, C.T., K. M. Rowe, D. Leneman, H. R. Lai, et al. (2019). InSight Auxiliary Payload Sensor Suite (APSS), *Space Sci Rev.*, *215*: 4. <https://doi.org/10.1007/s11214-018-0570-x>
- Banfield, D. et al. (2020) The atmosphere of Mars, as seen by InSight. *Nature Geoscience*, accepted. doi:10.1038/s41561-020-0534-0.
- Böse, M., Clinton, J. F., Ceylan, S., Euchner, F., van Driel, M., Khan, A., et al. (2017). A Probabilistic Framework for Single-Station Location of Seismicity on Earth and Mars. *Physics of the Earth and Planetary Interiors*, *262*, 48–65. <https://doi.org/10.1016/j.pepi.2016.11.003>
- Böse, M., Giardini, D., Stähler, S., Ceylan, S., Clinton, J., van Driel, M., et al. (2018). Magnitude scales for Marsquakes, *Bull. Seis. Soc. Am.* *108*(5A), 2764-2777, doi:10.1785/01201180037.
- Breuer, D., & Spohn, T. (2006). Viscosity of the Martian mantle and its initial temperature: Constraints from crust formation history and the evolution of the magnetic field. *Planetary and Space Science*, *54*(2), 153–169. <https://doi.org/10.1016/J.PSS.2005.08.008>
- Brown, J. R., & Roberts, G. P. (2019). Possible evidence for variation in magnitude for marsquakes from fallen boulder populations, Grjota Valles, Mars. *Journal of Geophysical Research: Planets*, *124*, 801– 822. <https://doi.org/10.1029/2018JE005622>.
- Brune, J. N. (1970). Tectonic stress and the spectra of seismic shear waves from earthquakes, *J. Geophys. Res.*, *75*(26), 4997–5009, doi:10.1029/JB075i026p04997.
- Clinton, J., Giardini, D., Böse, M., Ceylan, S., van Driel, M., Euchner, F. et al. (2018). The Marsquake Service: Securing Daily Analysis of SEIS Data and Building the Martian Seismicity Catalogue for InSight. *Space Science Review*, <https://doi.org/10.1007/s11214-018-0567-5>.
- Connolly, J. A. D. (2009). The geodynamic equation of state: What and how. *Geochemistry, Geophysics, Geosystems*, *10*(10), Q10014. <https://doi.org/10.1029/2009GC002540>
- Dreibus, G., & Wänke, H. (1984). Accretion of the Earth and the inner planets. In *Proceedings of the 27th International Geological Congress* (Vol. 11, pp. 1–20).
- Dumberry, M., & Rivoldini, A. (2015). Mercury’s inner core size and core-crystallization regime. *Icarus*, *248*, 254–268. <https://doi.org/10.1016/j.icarus.2014.10.038>
- Dziewonski, A. M., & Anderson, D. L. (1981). Preliminary reference Earth model. *Physics of the Earth and Planetary Interiors*, *25*(4), 297–356. [https://doi.org/10.1016/0031-9201\(81\)90046-7](https://doi.org/10.1016/0031-9201(81)90046-7)
- Genova, A., Goossens, S., Lemoine, F., Mazarico, E., Neumann, G., Smith, D. & Zuber, M. (2016). Seasonal and static gravity field of Mars from MGS, Mars Odyssey and MRO radio science, *Icarus*, Volume 272. doi: 10.1016/j.icarus.2016.02.050

- Golombek, M., & Phillips, R. (2009). Mars tectonics. In T. Watters & R. Schultz (Eds.), *Planetary Tectonics* (Cambridge Planetary Science, pp. 183-232). Cambridge: Cambridge University Press. doi:10.1017/CBO9780511691645.006
- Greeley, R. & Guest, J.E. (1987). Geologic map of the eastern equatorial region of Mars: U.S. Geological Survey Miscellaneous Investigations Series Map I-1802-B, scale 1:15,000,000.
- Green, R. G., Greenfield, T., White, R. S. (2015). Triggered earthquakes suppressed by an evolving stress shadow from a propagating dike. *Nature Geoscience*, 8(8), 629–632. <https://doi.org/10.1038/ngeo2491>
- Hauck, S. A., & Philipps, R. (2002). Thermal and crustal evolution of Mars. *Journal of Geophysical Research*, 107(E7), 5052. <https://doi.org/10.1029/2001JE001801>
- Jackson, I., & Faul, U. H. (2010). Grainsize-sensitive viscoelastic relaxation in olivine: Towards a robust laboratory-based model for seismological application. *Physics of the Earth and Planetary Interiors*, 183(1), 151–163, <https://doi.org/https://doi.org/10.1016/j.pepi.2010.09.005>
- Khan, A., Mosegaard, K., Williams, J. G., & Lognonné, P. (2004). Does the Moon possess a molten core? Probing the deep lunar interior using results from LLR and Lunar Prospector. *Journal of Geophysical Research (Planets)*, 109, 9007. <https://doi.org/10.1029/2004JE002294>
- Khan, A., van Driel, M., Böse, M., Giardini, D., Ceylan, S., Yan, J., et al. (2016). Single-station and single-event marsquake location and inversion for structure using synthetic Martian waveforms. *Physics of the Earth and Planetary Interiors*, 258, 28–42. <https://doi.org/10.1016/j.pepi.2016.05.017>
- Khan, A., Liebske, C., Rozel, A., Rivoldini, A., Nimmo, F., Connolly, J. A. D., et al. (2018). A Geophysical Perspective on the Bulk Composition of Mars. *Journal of Geophysical Research: Planets*, 1–37. <https://doi.org/10.1002/2017JE005371>
- Knapmeyer, M., Oberst, J., Hauber, E., Wählisch, M., Deuchler, C. & Wagner, R. (2006). Working models for spatial distribution and level of Mars' seismicity. *Journal of Geophysical Research: Planets* 111, 1–23. doi:10.1029/2006JE002708.
- Konopliv, A. S., Park, R. S., & Folkner, W. M. (2016). An improved JPL Mars gravity field and orientation from Mars orbiter and lander tracking data. *Icarus*, 274, 253–260.
- Lefort, A., Burr, D. M., Nimmo, F. & Jacobsen, R. E. (2015). Channel slope reversal near the Martian dichotomy boundary: Testing tectonic hypotheses. *Geomorphology*, 240, 121-136. <https://doi.org/10.1016/j.geomorph.2014.09.028>
- Lodders, K., & Fegley, B. (1997). An Oxygen Isotope Model for the Composition of Mars. *Icarus*, 126(2), 373–394. <https://doi.org/10.1006/ICAR.1996.5653>
- Lognonné et al. (2020). First constraints on the shallow elastic and anelastic structure of Mars from InSight data. *Nature Geoscience*, accepted. <http://doi.org/10.1038/s41561-020-0536-y>
- Mimoun, D., Murdoch, N., Lognonné, P., Hurst, K., Pike, W.T., Hurley, J., Nebut, T. & Banerdt, W.B. (2017). The Noise Model of the SEIS Seismometer of the InSight Mission to Mars, *Space Science Review*, doi: 10.1007/s11214-017-0409-x.
- Mohapatra, R. K., & Murty, S. V. (2003). Precursors of Mars: Constraints from nitrogen and oxygen isotopic compositions of martian meteorites. *Meteoritics & Planetary Science*, 38, 225–241. doi:10.1111/j.1945-5100.2003.tb00261.x

- Murdoch, M., Mimoun, D., Lognonné, P.H., and SEIS science team (2015a). SEIS performance model environment document, Tech. rep., ISGH-SEIS-JF-ISAE-030.
- Murdoch, M., Mimoun, D., Lognonné, P.H., and SEIS science team (2015b). SEIS performance budgets, Tech. rep., ISGH-SEIS-JF- ISAE-0010.
- Murdoch, N., Mimoun, D., Garcia, R.F., Rapin, W., Kawamura, T., Lognonné, P., Banfield, D. & Banerdt, W.B. (2017). Evaluating the Wind-Induced Mechanical Noise on the InSight Seismometers, *Space Science Review*, 211, 429-455, doi:10.1007/s11214-016-0311-y.
- Neukum, G., Jaumann, R., Hoffmann, H., Hauber, E., Head, J.W., Basilevsky, et al. (2004). Recent and episodic volcanic and glacial activity on Mars revealed by the High Resolution Stereo Camera. *Nature* 432, 971–979. doi:10.1038/nature03231
- Panning, M. P. et al. (2017), Planned Products of the Mars Structure Service for the InSight Mission to Mars, *Space Sci. Rev.*, 211(1), 611–650, doi:10.1007/s11214-016-0317-5.
- Plesa, A.-C., Grott, M., Tosi, N., Breuer, D., Spohn, T., & Wieczorek, M. A. (2016). How large are present-day heat flux variations across the surface of Mars? *Journal of Geophysical Research: Planets*, 121(12), 2386–2403. <https://doi.org/10.1002/2016JE005126>
- Rivoldini, A., Van Hoolst, T., Verhoeven, O., Mocquet, A., & Dehant, V. (2011). Geodesy constraints on the interior structure and composition of Mars. *Icarus*, 213(2), 451–472. <https://doi.org/10.1016/j.icarus.2011.03.024>
- Rubin, A. M., & Gillard, D. (1998). Dike-induced earthquakes: Theoretical considerations. *Journal of Geophysical Research*, 103(1), 17–30.
- Samuel, H., Lognonné, P., Panning, M. P., & Lainey, V. (2019). The rheology and thermal history of Mars revealed by the orbital evolution of Phobos. *Nature*, 569(7757), 523–527. <https://doi.org/10.1038/s41586-019-1202-7>
- Sanloup, C., Jambon, A., & Gillet, P. (1999). A simple chondritic model of Mars. *Physics of the Earth and Planetary Interiors*, 112(1–2), 43–54. [https://doi.org/10.1016/S0031-9201\(98\)00175-7](https://doi.org/10.1016/S0031-9201(98)00175-7)
- Sigmundsson, F., Hooper, A., Hreinsdóttir, S., Vogfjörð, K. S., Ófeigsson, B. G., Heimisson, E. R., et al. (2015). Segmented lateral dike growth in a rifting event at Bárðarbunga volcanic system, Iceland. *Nature*, 517(7533), 191–195. <https://doi.org/10.1038/nature14111>
- Smrekar, S. E., Lognonné, P., Spohn, T., Banerdt, W. B., Breuer, D., Christensen, U., et al. (2019). Pre-mission InSights on the Interior of Mars. *Space Science Reviews*, 215(1), 3. <https://doi.org/10.1007/s11214-018-0563-9>
- Stixrude, L., & Lithgow-Bertelloni, C. (2005). Thermodynamics of mantle minerals - I. Physical properties. *Geophysical Journal International*. <https://doi.org/10.1111/j.1365-246X.2005.02642.x>
- Stixrude, L., & Lithgow-Bertelloni, C. (2011). Thermodynamics of mantle minerals - II. Phase equilibria. *Geophysical Journal International*, 184, 1180–1213. <https://doi.org/10.1111/j.1365-246X.2010.04890.x>
- Taylor, G. J. (2013). The bulk composition of Mars. *Chemie der Erde - Geochemistry*, 73(4), 401–420. <https://doi.org/10.1016/J.CHEMER.2013.09.006>



- Taylor, G. J., Stopar, J. D., Boynton, W. V., Karunatillake, S., Keller, J. M., Brückner, J., et al. (2006). Variations in K/Th on Mars. *Journal of Geophysical Research*, 112(E3), E03S06. <https://doi.org/10.1029/2006JE002676>
- Taylor, J., Teanby, N. A., & Wookey, J. (2013). Estimates of seismic activity in the Cerberus Fossae region of Mars. *Journal of Geophysical Research: Planets*, 118(12), 2570-2581.
- Taylor, S. R. (1980). Refractory and moderately volatile element abundances in the earth, moon and meteorites. In S. A. Bedini (Ed.), *Lunar and Planetary Science Conference Proceedings* (Vol. 11, pp. 333–348).
- Thiriet, M., Michaut, C., Breuer, D., & Plesa, A.-C. (2018). Hemispheric Dichotomy in Lithosphere Thickness on Mars Caused by Differences in Crustal Structure and Composition. *Journal of Geophysical Research: Planets*. <https://doi.org/10.1002/2017JE005431>
- Vaucher, J., Baratoux, D., Mangold, N., Pinet, P., Kurita, K., & Grégoire, M. (2009). The volcanic history of central Elysium Planitia: Implications for martian magmatism. *Icarus*, Volume 204. doi: 10.1016/j.icarus.2009.06.032.
- Wieczorek, M. A., & Zuber, M. T. (2004). Thickness of the Martian crust: Improved constraints from geoid-to-topography ratios. *Journal of Geophysical Research*, 109(E1), E01009. <https://doi.org/10.1029/2003JE002153>
- Zuber, M., Solomon, S., Phillips, R., Smith, D., Tyler, L., Aharonson, O., et al. (2000). Internal Structure and Early Thermal Evolution of Mars from Mars Global Surveyor Topography and Gravity, *Science*, Volume 287. doi: 10.1126/science.287.5459.1788.